

Advanced Palladium Nanosheet-Enhanced Phototherapy for Treating Wound Infection Caused by Multidrug-Resistant Bacteria

Shanshan Li, Mingzhu Lu, Chenxi Dai, Bolong Xu, Nier Wu, Lin Wang, Chao Liu, Fangzhou Chen, Haokun Yang, Zhijun Huang, Huiyu Liu,* and Dongsheng Zhou*

With the increasing spread of multidrug-resistant (MDR) bacteria worldwide, it is needed to develop antibiotics-alternative strategies for the treatment of bacterial infections. This work develops a multifunctional single-component palladium nanosheet (PdNS) with broad-spectrum and highly effective bactericidal activity against MDR bacteria. PdNS exerts its endogenous nanoknife (mechanical cutting) effect and peroxidase-like activity independent of light. Under near-infrared region (NIR) light irradiation, PdNS exhibits photothermal effect to produce local heat and meanwhile possesses photodynamic effect to generate $^1\text{O}_2$; notably, PdNS has catalase-like activity-dependent extra photodynamic effect upon H_2O_2 addition. PdNS+ H_2O_2 +NIR employs a collectively synergistic mechanism of nanoknife effect, peroxidase/catalase-like catalytic activity, photothermal effect, and photodynamic effect for bacterial killing. PdNS+ H_2O_2 +NIR causes compensatory elevated phospholipid biosynthesis, disordered energy metabolism, increased cellular ROS levels and excessive oxidative stress, and inhibited nucleic acid synthesis in bacteria. In mice, PdNS+ H_2O_2 +NIR gives >92.7% bactericidal rates at infected wounds and almost the full recovery of infected wounds, and it leads to extensive down-regulation of proinflammatory pathways and comprehensive up-regulation of wound healing pathways, conferring elevated inflammation resolution and meanwhile accelerated wound repair. PdNS+ H_2O_2 +NIR represents a highly efficient nanoplatform for photoenhanced treatment of superficial infections.

development of antibiotic resistance in bacteria is related to two major contributors, namely incorrect DNA replication leading to generation of antibiotics-insensitive mutants, and horizontal transfer of resistance genes.^[1] The World Health Organization (WHO) has included antimicrobial resistance as one of the top 10 threats to global health and listed a cluster of ESKAPE pathogens, including *Enterococcus faecium* (*Ec. faecium*), *Staphylococcus aureus* (*S. aureus*), *Klebsiella pneumoniae* (*K. pneumoniae*), *Acinetobacter baumannii* (*A. baumannii*), *Pseudomonas aeruginosa* (*P. aeruginosa*), and *Enterobacteriaceae* species (such as *Eb. Hormaechei*), which have been given the highest priority status owing to their elevated resistance and virulence.^[2] Currently, bacterial infection treatment in clinical practice relies heavily on antibiotics, but the discovery and clinical approval of novel antibiotics are too slow to tackle the rapid emergence of MDR.^[3] As a result, there is an urgent need to develop antibiotics-alternative antimicrobial agents (such as nanomaterials) against MDR bacteria, particularly ESKAPE superbugs.^[4]

Given their multifunctional features, inorganic nanomaterials have been applied in various fields such as biomedicine,^[5]

energy,^[6] and catalysis.^[7] When used as antibacterial agents, nanomaterials can evade existing resistance mechanisms and thus be less prone to select for resistance than conventional

1. Introduction

With the overuse and misuse of antibiotics, multidrug-resistant (MDR) bacteria have increasingly spread worldwide. The rapid

S. Li, B. Xu, C. Liu, H. Yang, Z. Huang, H. Liu
Beijing Advanced Innovation Center for Soft Matter Science and Engineering
State Key Laboratory of Organic-Inorganic Composites
Bionanomaterials & Translational Engineering Laboratory
Beijing Key Laboratory of Bioprocess
Beijing Laboratory of Biomedical Materials
Beijing University of Chemical Technology
Beijing 100029, China
E-mail: liuhy@mail.buct.edu.cn

M. Lu, C. Dai, N. Wu, L. Wang, F. Chen, D. Zhou
State Key Laboratory of Pathogen and Biosecurity
Academy of Military Medical Sciences
Beijing 100071, China
E-mail: zhouds@bmi.ac.cn
L. Wang
Northern Medical Branch of PLA General Hospital
Beijing 100094, China

 The ORCID identification number(s) for the author(s) of this article can be found under <https://doi.org/10.1002/sml.202407180>

DOI: 10.1002/sml.202407180

antibiotics. Additionally, their unique size, surface potential, hydrophilicity, and dimensions give them the potency to adhere to bacterial cells.^[8] One of the most widely studied inorganic nanoantibacterial agents is silver nanoparticles^[9] and other kinds of metal (such as iron, copper, zinc, cobalt, nickel, and ruthenium) nanoparticles have also been reported to possess antibacterial effects,^[10] all of which are mainly attributable to metal ion-mediated chemodynamic effect that employs Fenton or Fenton-like reactions for generating more toxic •OH from endogenous H₂O₂. Moreover, external field-responsive nanomaterials allow them to achieve antibacterial efficacy through sonodynamic effect that utilizes low-intensity focused ultrasound to excite sonosensitizers to generate reactive oxygen species (ROS),^[11] photodynamic effect that harnesses the energy of near-infrared region (NIR) light through photosensitizers to generate ROS,^[12] or photothermal effect that exploits photothermal agents to absorb energy from NIR light for producing heat.^[13] Construction of heterostructures or spatially asymmetric Janus structures will greatly promote the migration of carriers as well as the separation of electron–hole pairs, which will lead to the elevated oxidation and reduction reactions in electron- and hole-rich regions respectively, or the improved thermal motion of electrons thereby enhancing the yield of ROS or heat, respectively.^[11–13] However, constructing the hybrids of semiconductor/semiconductor, semiconductor/noble metal, and noble/noble metal will increase the difficulty and cost of nanomaterial preparation, and additionally bring concerns regarding the stability and controllability of these hybrid nanosystems.^[11–13]

It has been reported that 2D nanosheets have the unique nanoknife effect to improve bactericidal efficacy owing to mechanical cutting on bacterial cells, and this nanoknife effect is correlated to the sizes of nanosheets.^[14] Inspired by this, we developed a multi-functional single-component palladium nanosheet (PdNS), which exhibited broad-spectrum and highly effective bactericidal activity against MDR ESKAPE pathogens via the synergistic action of its intrinsic nanoknife effect, enzyme-like activities, and NIR-triggered photothermal and photodynamic effects (Scheme 1). PdNS was highly efficient for photo-enhanced treatment of infected wounds in mice caused by MDR bacteria.

2. Results and Discussion

2.1. Preparation and Characterization of PdNS

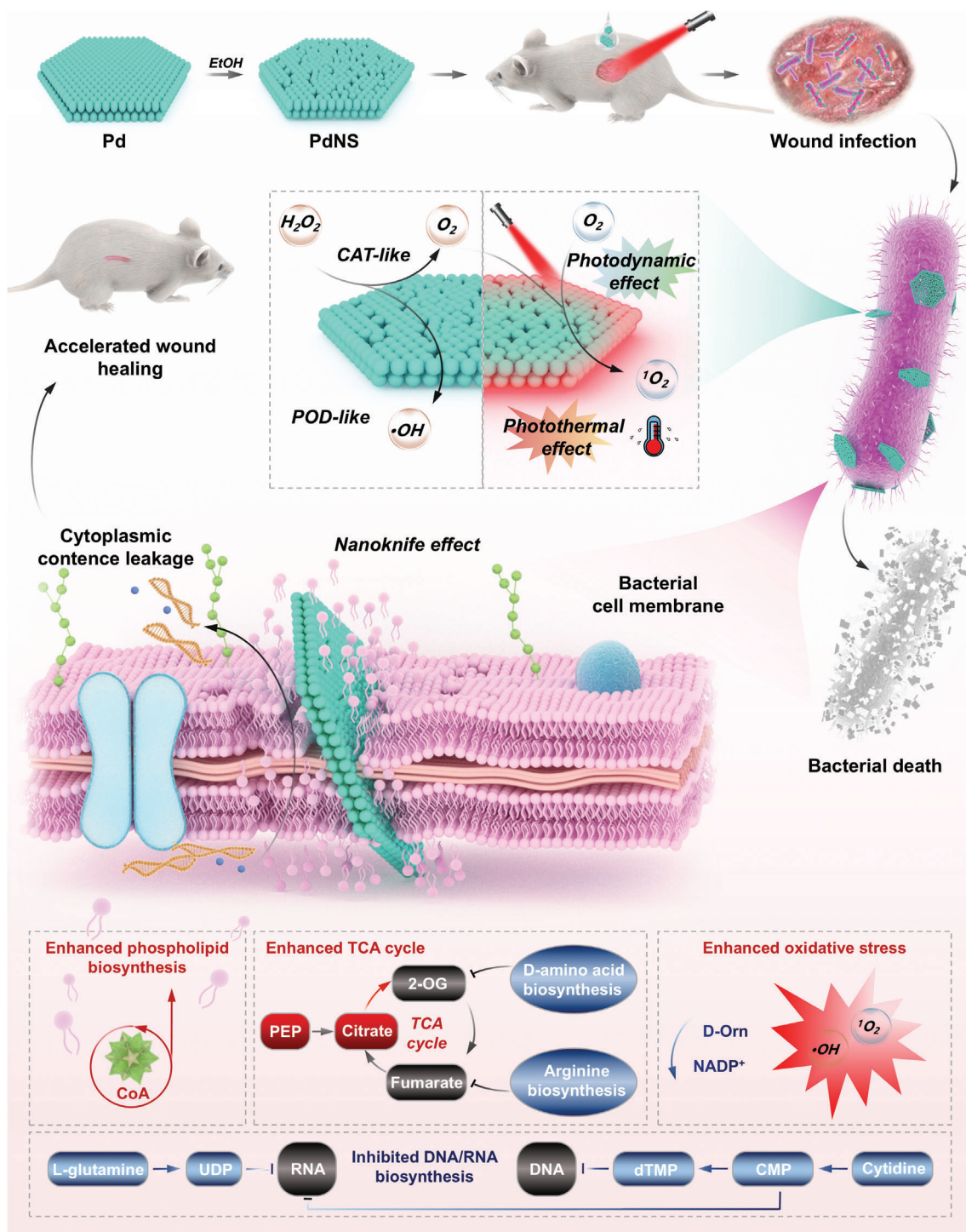
As described in our previous study,^[15] Pd nanosheet (PdNS) was synthesized through the reduction of palladium acetylacetonate [Pd(acac)₂] under a CO (0.5 MPa) atmosphere, Poly(vinylpyrrolidone) (PVP) and Br[−] were added as the coating agent and structure-directing agents, respectively. Transmission electron microscope (TEM) revealed that PdNS had a good monodispersity (Figure 1a) and exhibited an irregular hexagonal lamellar structure with a rough surface (Figure 1b). Compared to PdNS reported earlier,^[15] the average size of PdNS in this work was reduced from about 130 nm to around 48 nm in width as measured by TEM (Figure 1b). The hydrated particle size was about 51 nm (PDI: 0.228) as measured by dynamic light scattering (DLS) (Figure 1c). As determined by the atomic force microscope (AFM), the thicknesses of PdNS ranged from 2 to 3 nm (Figure 1d–f), likely owing to the flexibility in thicknesses of PVP

coated on the PdNS's surface. Collectively, the smaller particle size (about 48 nm) was expected to facilitate the attachment of PdNS to the bacterial cell surface due to the accelerated molecular thermal motion and the reduced spatial potential resistance, while the extremely thin thickness (2–3 nm) was expected to provide a prerequisite for the mechanical cutting function of PdNS against bacteria.

The zeta potential of PdNS was −11.5 mV (Figure S1, Supporting Information). The surface chemical properties and electronic configurations of PdNS were then detected by X-ray photoelectron spectroscopy (XPS), and the XPS spectrum (Figure 1g) denoted the presence of elements O, C, N, and Pd, among which O, C, and N were attributed to PVP coating on PdNS's surface. Pd 3d spectra exhibit two discernible peaks at the binding energy of 340.27 eV and 334.87 eV, which correspond to the spin-orbit splitting of Pd⁰ 3d_{3/2} and Pd⁰ 3d_{5/2} species, respectively (Figure 1h). X-ray diffraction (XRD) was employed to analyze the crystal structure of PdNS, identifying a prominent peak at 2θ approximately 67.9° corresponding to the (220) facet. Additionally, the distinct peaks at 2θ around 39.4° and 45.1° were attributed to the diffraction peaks of (111) and (200) planes, respectively (Figure 1i).

2.2. Photo Responsiveness of PdNS

NIR light is considered to be a safer light source for phototherapy in humans.^[16] Photo responsiveness of PdNS in vitro upon 808 nm laser irradiation was systematically characterized herein. First, the light absorption characteristics of PdNS were assessed based on the electronic structure of noble metal atoms and their responsiveness to light. As shown in Figure 2a, PdNS exhibited prominent and wide-ranging absorption bands across the whole NIR region. Second, the photothermal properties of PdNS were evaluated. The temperatures of PdNS at 12.5 to 50 μg mL^{−1} in the aqueous solution were increased rapidly upon 808 nm laser irradiation (1.5 W cm^{−2}), and the temperature of 50 μg mL^{−1} PdNS reached 67.7 °C after 5 min irradiation (Figure 2b). This temperature increment was virtually observed by infrared images (Figure 2c). Third, the catalase-like activity of PdNS to decompose H₂O₂ into O₂ was further detected by using a dissolved oxygen meter. After dropping H₂O₂ (3.2 mM) into the PdNS solution (10 μg mL^{−1}, pH = 7.4), the amount of dissolved oxygen in the buffer continued to rise and reached 19.1 mg L^{−1} 5 min later (Figure S2, Supporting Information). Fourth, the NIR-induced photodynamic properties of PdNS were assessed. As revealed by ESR measurements, a 4.76-fold increase in singlet oxygen (¹O₂) signal was observed for the PdNS+NIR group compared to the Control+NIR group; the addition of H₂O₂ into the system further enhanced the ¹O₂ signal, which could be attributed to O₂ generation mediated by the catalase-like activity of PdNS (Figure 2d). To further confirm ¹O₂ production, 9,10-diphenylanthracene (DPA) was utilized to directly detect ¹O₂ through its degradation, leveraging its reactivity with ¹O₂ to generate endoperoxides.^[17] As shown in Figure 2e,f, there was a significant decrease in the absorption values of DPA with the prolonging of irradiation times, confirming that PdNS promoted the production of ¹O₂ under NIR laser irradiation. Taken together, PdNS under NIR irradiation displayed the excellent photothermal effect to generate local heat as well as the outstanding photodynamic effect to produce



Scheme 1. Schematic illustration of photo-responsive antibacterial action of PdNS. PdNS alone exerts basal bactericidal activity due to its intrinsic nanoknife effect and peroxidase-like activity, which is independent of NIR light. PdNS+NIR shows significantly enhanced bactericidal activity due to the cooperative action of the endogenous nanoknife effect (most) and peroxidase-like activity (little), and the NIR-induced photothermal and photodynamic effects. PdNS+H₂O₂+NIR displays the best bactericidal activity because of catalase-like enzyme-dependent extra photodynamic activity upon H₂O₂ addition. Through a collectively synergistic mechanism of nanoknife effect, peroxidase/catalase-like catalytic activity, photothermal effect, and photodynamic effect, PdNS+H₂O₂+NIR exhibited highly bactericidal action, and from the perspective of bacterial metabolic change, it causes compensatory elevated phospholipid biosynthesis, disordered energy metabolism, increased cellular ROS levels and excessive oxidative stress, and inhibited nucleic acid synthesis in bacteria. PdNS+H₂O₂+NIR is highly efficient for the photo-enhanced treatment of infected wounds in mice caused by MDR bacteria, and this therapeutic platform could lead to extensive down-regulation of pro-inflammatory pathways and comprehensive up-regulation of wound healing pathways at infected wounds as viewed from host transcriptomic change, conferring elevated inflammation resolution as well accelerated wound repair.

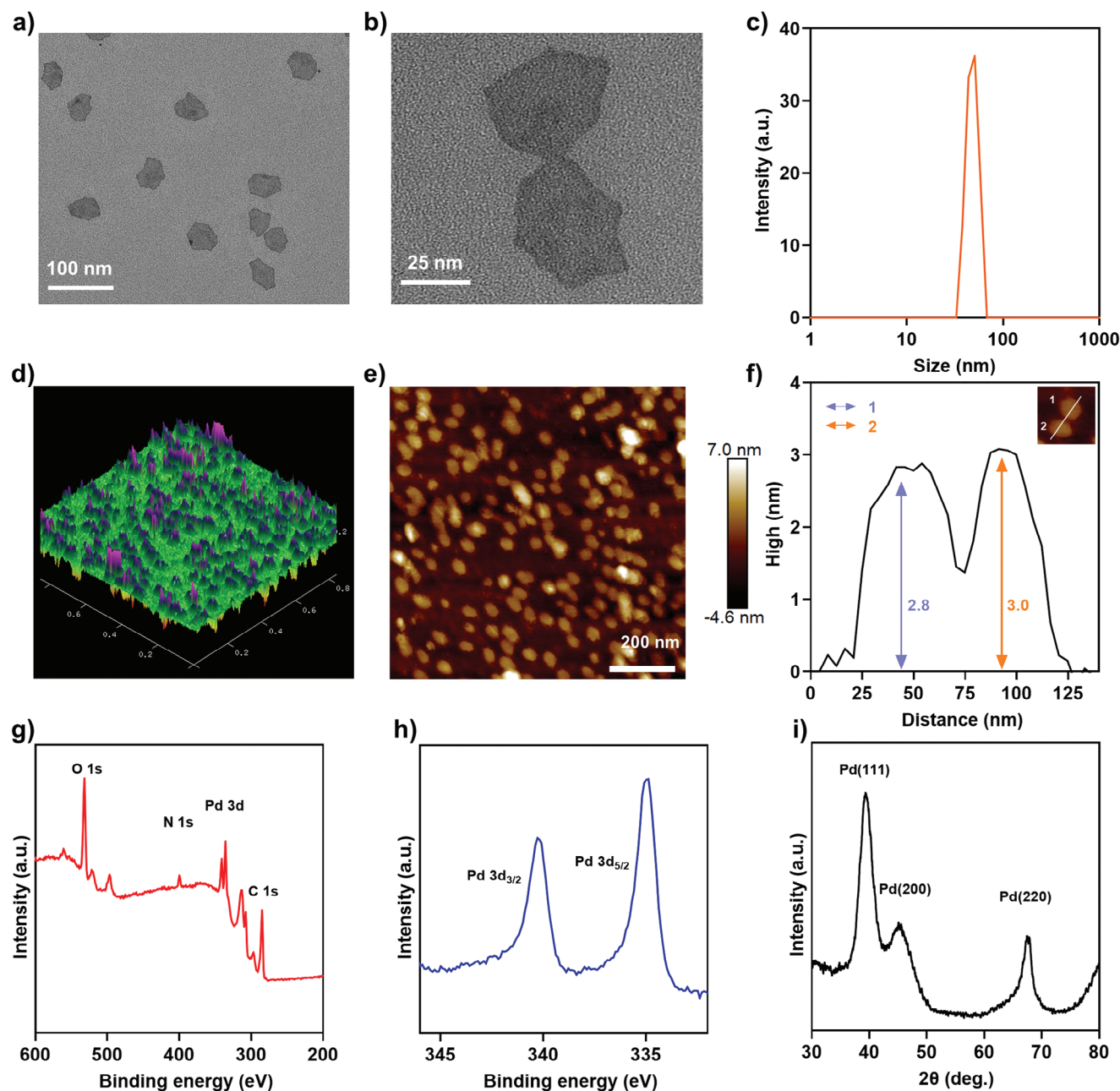


Figure 1. Structural characterization of PdNS. a,b) TEM images of PdNS. c) Size distribution of PdNS as determined by DLS. d) 3D AFM image of PdNS. e) 2D AFM image of PdNS. f) Thickness distribution curves of PdNS detected by AFM. g) XPS survey spectra of PdNS. h) Pd 3d XPS spectrum of PdNS. i) XRD pattern of PdNS.

$^1\text{O}_2$; notably, PdNS possessed the intrinsic catalase-like activity to generate O_2 in the presence of H_2O_2 and thus it would exhibit the extra photodynamic activity upon H_2O_2 addition.

2.3. Photo-Enhanced Broad-Spectrum Antibacterial Activity of PdNS In Vitro

A total of 8 treatment groups (Control, Control+NIR, H_2O_2 , H_2O_2 +NIR, PdNS, PdNS+NIR, PdNS+ H_2O_2 , and

PdNS+ H_2O_2 +NIR) were settled to examine in vitro inhibition rates against 6 clinical MDR isolates of ESKAPE pathogens, including Gram-positive *Ec. Faecium* HJP554,^[18] and *S. aureus* USA300-FPR3757,^[19] and Gram-negative *K. pneumoniae* ATCC BAA-2146,^[20] *A. baumannii* LAC-4,^[21] *P. aeruginosa* F291007,^[18] and *Eb. Hormaechei* ATCC BAA-2082 (<https://www.atcc.org/products/baa-2082>). The representative plate counting images after different treatments and the corresponding statistical data of bacterial colony counts were presented in **Figure 3**. For these 6 ESKAPE isolates, the PdNS

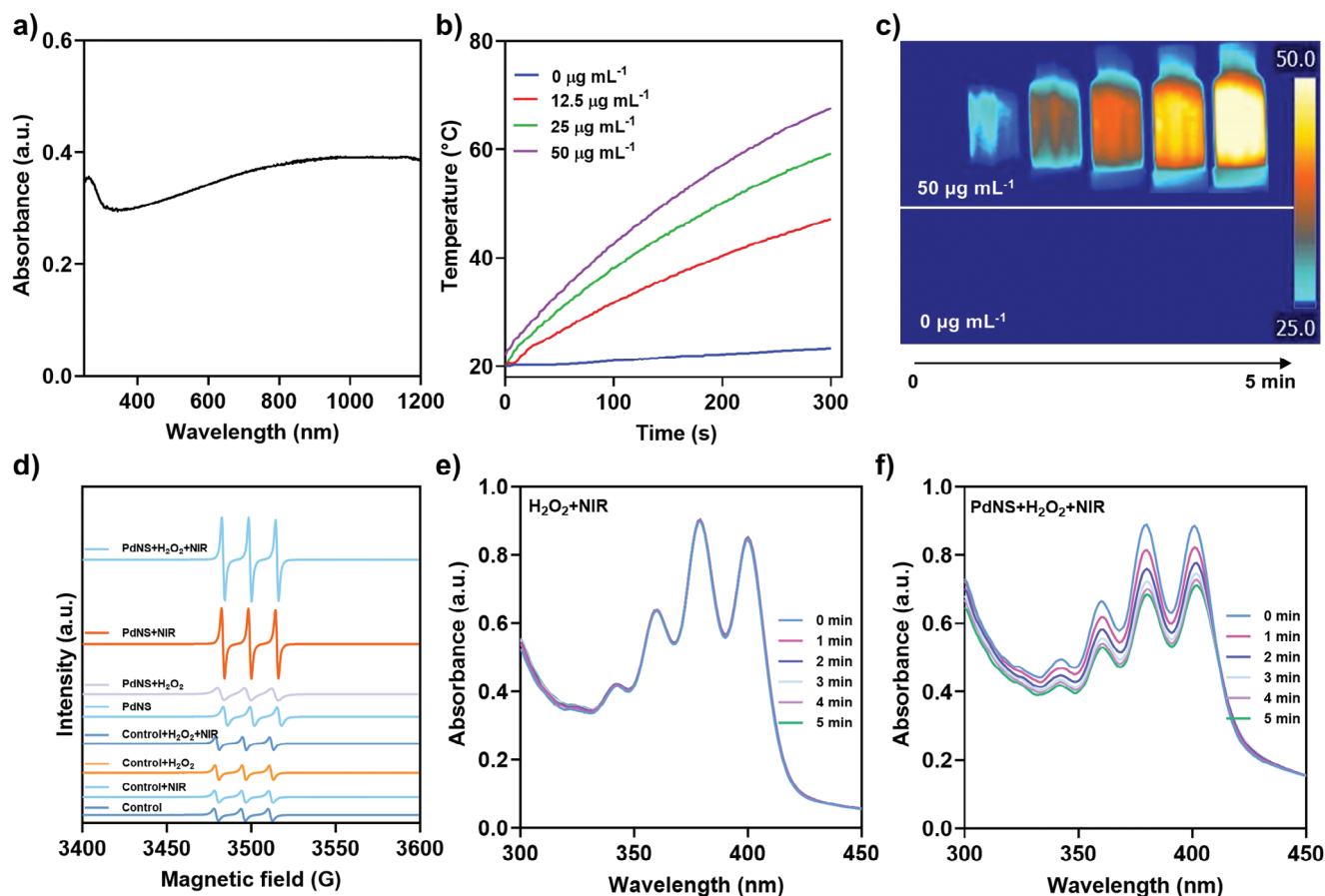


Figure 2. Photoresponsive performance of PdNS. a) UV-Vis-NIR absorption spectrum of PdNS. b) Concentration-dependent temperature curves of PdNS aqueous solutions upon 808 nm laser irradiation (1.5 W cm^{-2} , 5 min). c) Infrared thermal images of the water solution and the $50 \mu\text{g mL}^{-1}$ PdNS aqueous solution. d) ESR measurement of the photodynamic property of PdNS. e, f) DPA degradation for detecting PdNS-dependent $^1\text{O}_2$ generation. Control stands for d) ethanol, or e, f) PBS. PdNS corresponds to $50 \mu\text{g mL}^{-1}$ of PdNS. NIR represents 808 nm laser irradiation (1.5 W cm^{-2} , 5 min). H_2O_2 denotes the addition of d) 0.2 mM or e–f) 8 mM H_2O_2 .

group showed 18.9%–67.0% inhibition rates, which might result from the nanoknife effect together with the enzyme-like activities of PdNS; the PdNS+NIR group gave increased inhibition rates 73.8%–94.03%, likely owing to the combined action of nanoknife effect, enzyme-like activities, photothermal effect, and photodynamic effect; PdNS+ H_2O_2 +NIR exhibited further elevated inhibition rates at >99.2%, probably because of extra photodynamic effect upon H_2O_2 addition.

2.4. Mechanism of Antibacterial Activity of PdNS In Vitro

Based on the above in vitro antimicrobial experiments, we speculated that the antimicrobial mechanisms employed by PdNS+ H_2O_2 +NIR might mainly include photothermal effect, photodynamic effect, nanoknife effect, and enzyme-like catalysis, which were systematically explored herein using *S. aureus* and *P. aeruginosa* as the model bacteria. First, to primarily verify the nanoknife effect, PdNS alone at different concentrations was incubated with *S. aureus*, and the inhibition rates were determined by the plate counting method; as expected, the inhibition rates were gradually increased with the enhancement of

PdNS concentrations and the prolonging of incubation times (Figure S3, Supporting Information). Second, to further differentiate the roles between the nanoknife effect and the peroxidase-like catalytic activity of PdNS, we added excess vitamin C ($200 \mu\text{g mL}^{-1}$) to the suspension of *S. aureus* treated by the PdNS or PdNS+ H_2O_2 group in the dark to offset ROS generation. As shown in Figure S4 (Supporting Information), after adding vitamin C, the inhibition rate of PdNS remained at above 80%; therefore, the basal bactericidal activity of PdNS in the absence of light was principally dependent on its endogenous nanoknife effect although its peroxidase-like catalytic activity might play a minor role. Third, the cytoplasmic DNA and K^+ in the supernatants of bacterial suspensions after different treatments were then measured, given that the damage to bacterial cell membrane would lead to the leakage of bacterial cytoplasmic components.^[22] As shown in Figure 4a–d, DNA and K^+ contents were detected at similar levels in the PdNS and PdNS+ H_2O_2 groups, confirming the nanoknife effect; relatively, much higher DNA and K^+ contents were observed in the PdNS+NIR group, confirming the photothermal and photodynamic effects of PdNS; in addition, the PdNS+ H_2O_2 +NIR group gave the highest DNA and K^+ levels, confirming that the photothermal activity of PdNS was enhance

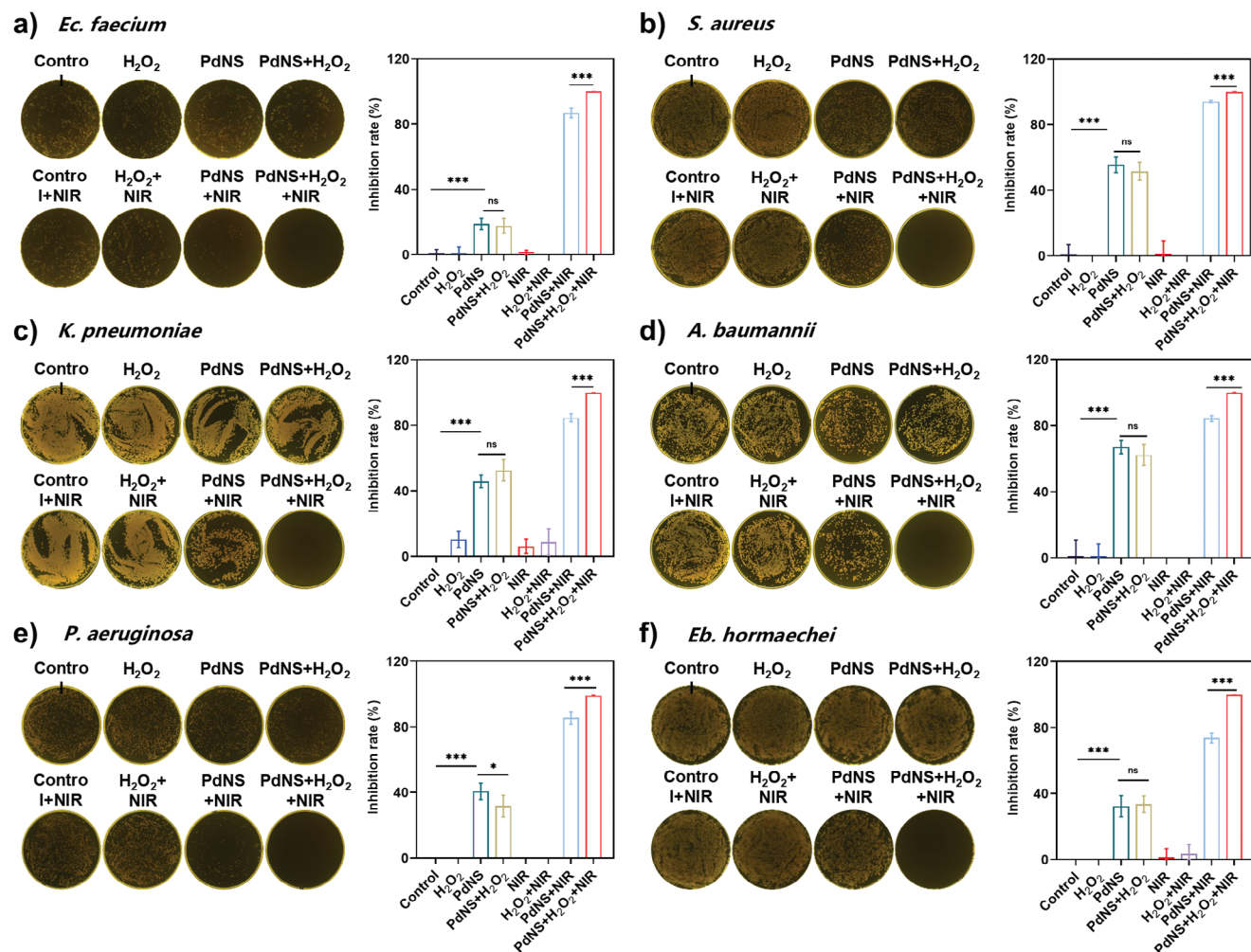


Figure 3. Broad-spectrum in vitro antibacterial efficacy of PdNS against ESKAPE pathogens, including a) *E. faecium*, b) *S. aureus*, c) *K. pneumoniae*, d) *A. baumannii*, e) *P. aeruginosa*, and f) *Eb. Hormaechei*. Control refers to PBS. PdNS refers to 50 $\mu\text{g mL}^{-1}$ PdNS. NIR represents 808 nm laser irradiation (1.5 W cm^{-2} , 3 min). H₂O₂ denotes the addition of $1 \times 10^{-3} \text{ M}$ H₂O₂. Data are presented as mean \pm SD ($n = 5$). ns: $P \geq 0.05$, *: $P < 0.05$, **: $P < 0.01$, ***: $P < 0.001$.

upon H₂O₂ addition. Fourth, the 2,7-dichlorodihydrofluorescein diacetate (DCFH-DA) probe was used to detect the peroxidase-like activity of PdNS. As shown in Figure 4e,f, significant fluorescence enhancement was detected for the PdNS or PdNS+H₂O₂ group relative to the Control group, which could be attributed to the peroxidase-like activity of PdNS. However, no significant difference could be found between the PdNS and PdNS+H₂O₂ groups, and it was thought that the relatively neutral pH under rational bacterial culture conditions inhibited the peroxidase-like activity of PdNS and promoted its catalase-like activity, so most of H₂O₂ added in the system for the PdNS+H₂O₂ group would be decomposed into O₂, resulting in no significant increase. Fifth, the morphology of bacteria after different treatments was observed by using TEM (Figure S5a, Supporting Information) and scanning electron microscope (SEM, Figure S5b, Supporting Information). For the PdNS and PdNS+H₂O₂ groups, the edges of bacteria cells became roughened, and obvious heterogeneous structure existed on bacterial surfaces (yellow arrow), and even the insertion of PdNS into bacterial cells membrane could be

observed (red arrow); in the PdNS+NIR and PdNS+H₂O₂+NIR groups, the severe collapse of bacteria cells could be observed. Sixth, SYTO-9/propidium iodide dyes were further applied to detect the percentages of dead bacteria. For *S. aureus*, the percentages were 43.5%, 39.0%, 87.0%, and 89.2% for the PdNS, PdNS+H₂O₂, PdNS+NIR, and PdNS+H₂O₂+NIR groups, respectively (Figure 4g). For *P. aeruginosa*, the corresponding percentages were 17.9%, 17.9%, 66.4%, and 69.1% (Figure 4h). The fluorescence images of dead (red) and live (green) bacteria were also captured by confocal laser scanning microscopy (CLSM) (Figure 4i). Collectively, compared to PdNS alone that showed basal bactericidal activity owing to its intrinsic nanoknife effect (most) and peroxidase-like activity (little), PdNS+NIR gave significantly enhanced bactericidal activity due to the cooperative action of the endogenous nanoknife effect and peroxidase-like activity, and the NIR-induced photothermal and photodynamic effects, while PdNS+H₂O₂+NIR displayed the best bactericidal activity because of catalase-like enzyme-dependent extra photodynamic activity upon H₂O₂ addition.

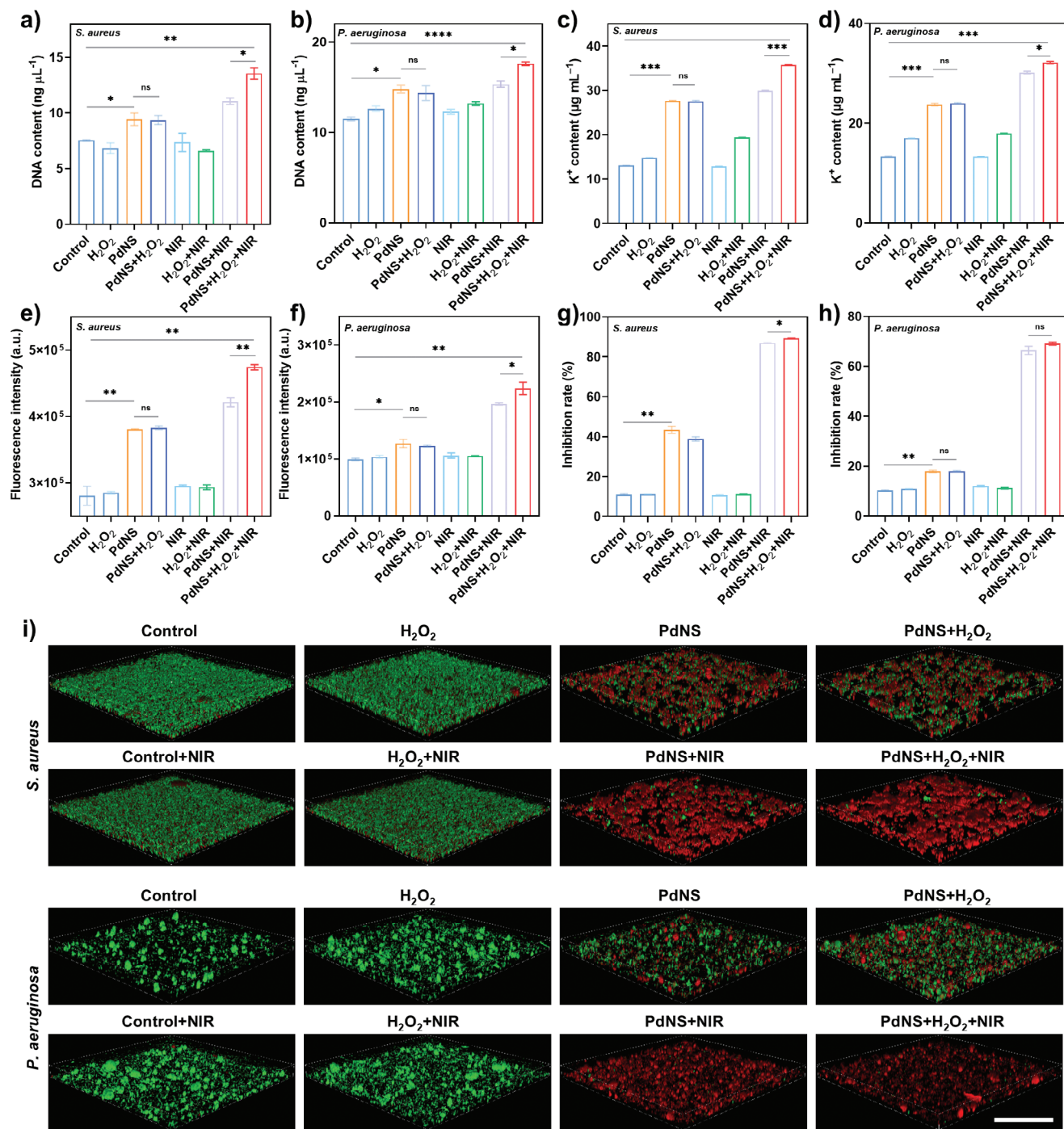


Figure 4. Antibacterial mechanisms of PdNS in vitro. Leakage of cytoplasmic DNA for a) *S. aureus* and b) *P. aeruginosa* after different treatments. Leakage of cytoplasmic K⁺ for c) *S. aureus* and d) *P. aeruginosa* after different treatments. Fluorescence intensity of ROS generated by e) *S. aureus* and f) *P. aeruginosa* after different treatments. Fluorescence intensity percentage of dead *S. aureus* g) and *P. aeruginosa* h) after different treatments. Control stands for PBS. PdNS corresponds to 50 $\mu\text{g mL}^{-1}$ PdNS. NIR represents 808 nm laser irradiation (1.5 W cm^{-2} , 3 min). H₂O₂ denotes the addition of 1 mM H₂O₂. Data are presented as mean \pm SD (n = 3). ns: $P \geq 0.05$, *: $P < 0.05$, **: $P < 0.01$, ***: $P < 0.001$. i) Living/dead double staining of *S. aureus* and *P. aeruginosa* after different treatments. Scale bar = 100 μm .

To better understand the bactericidal mechanism of PdNS *in vitro*, the metabolomes of *S. aureus* were compared between the PdNS+H₂O₂+NIR and Control groups. First, principal component analysis (PCA) was used to reveal the internal structure between the two groups. As shown in **Figure 5a**, 6 individual samples in each group were scattered in two datasets, indicating that there was a significant difference between the two datasets and the samples within each group showed good repeatability. Second, a total of 296 differentially regulated metabolites (DRMs) were identified for PdNS+H₂O₂+NIR relative to Control (**Figure 5b**), of which 105 were up-regulated and 191 were down-regulated. Third, KEGG (Kyoto Encyclopedia of Genes and Genomes) pathway enrichment analysis identified 5 enriched up-regulated pathways including pantothenate and CoA biosynthesis, starch and sucrose metabolism, thiamine metabolism, tricarboxylic acid cycle (TCA cycle), galactose metabolism, and also 5 enriched down-regulated pathways including pyrimidine metabolism, D-amino acid metabolism, arginine biosynthesis, glutathione metabolism, and biosynthesis of various other secondary metabolites (**Figure 5c**). Fourth, 20 selected DRMs (including 8 up-regulated ones and 12 down-regulated ones, **Figure 5d**) and 7 corresponding biochemical processes (**Figure 5e**) were mapped to clarify the principal metabolic responses of *S. aureus* post treatment: i) the up-regulation of 4 different phospholipid biosynthesis-related metabolites denoted that the damage of PdNS+H₂O₂+NIR to bacterial cell membrane would induce the compensatory elevation of phospholipid biosynthesis pathway;^[23] ii) the down-regulation of NADP⁺ and L-ornithine indicated the excessive oxidative stress;^[24] iii) the down-regulation L-ornithine, D-ornithine, and D-glutamine (involved in D-amino acid metabolism), and N-acetylornithine, and L-glutamine (responsible for arginine biosynthesis) would directly affect the homeostasis of TCA cycle, which was consistent with the up-regulation of phosphoenolpyruvate and citrate to maintain energy supply, and suggested the disordered energy metabolism;^[25] iv) the down-regulation of L-glutamine, UDP, cytidine, CMP, and dTMP indicated the inhibition of RNA/DNA synthesis. Taken together, PdNS+H₂O₂+NIR lead to elevation of phospholipid biosynthesis (compensatory to bacterial cell membrane damage), the disorder of energy metabolism (related to elevated TCA cycle and inhibited D-amino acid metabolism and arginine biosynthesis), increased cellular ROS levels and excessive oxidative stress, and inhibition of RNA/DNA synthesis in bacteria.

2.5. Therapeutic Efficacy of PdNS Against Infected Wounds in Mice

To test the *in vivo* therapeutic capability of PdNS, *S. aureus* (**Figure 6**) or *P. aeruginosa* (**Figure S6**, Supporting Information) was inoculated in mice wounds to establish bacterial infection, which was then treated with a total of 6 groups including Control, PdNS, PdNS+H₂O₂, NIR, PdNS+NIR, and PdNS+H₂O₂+NIR. The H₂O₂ and H₂O₂+NIR groups gave similar antibacterial activities as the Control group in the above *in vitro* antimicrobial experiments, and thus these two groups were excluded herein. First, as shown in **Figures 6a,b** and **S6a,b** (Supporting Information), the local temperatures at infected wounds

treated by PdNS+NIR and PdNS+H₂O₂+NIR were increased gradually with the extension of irradiation times, confirming excellent NIR-induced photothermal effect *in vivo*. Second, the wound areas were photographed and measured every 2 days post-therapy, and the corresponding statistical data were presented in **Figures 6c,d** and **S6c,d** and **Figure S7** (Supporting Information); PdNS+H₂O₂+NIR gave the best therapeutic effect with almost 100% recovery of infected wounds on day 8 post-therapy. As expected, the healing speeds for infected wounds gave the following statistically different trend: PdNS+H₂O₂+NIR > PdNS+NIR > PdNS (**Figure S8**, Supporting Information). Third, the body weights of mice were recorded for the 6 groups (**Figures 6e** and **S6e** Supporting Information), and the results showed that there was no obvious weight loss in all these groups. Additionally, there was the detection of > 90% cell viability of NIH3T3 mouse embryonic normal fibroblast cells after different treatment with 200 μg mL⁻¹ PdNS for 24 h by using MTT assay (**Figure S9**, Supporting Information), as well as the observation of no obvious pathological lesions in the heart, liver, spleen, lung, and kidney of mice with *S. aureus*- or *P. aeruginosa*-infected wounds on day 8 post-therapy by using hematoxylin & Eosin (H&E) staining (**Figure S10**, Supporting Information). These results confirmed the highly favored biosafety of PdNS at both cellular and animal levels. Fourth, on day 2 post-therapy, the wound tissues were collected and homogenized to detect bacterial loads at wound sites (**Figures 6f,g** and **S6f,g**, Supporting Information), giving the as-expected statistically different trend: PdNS+H₂O₂+NIR < PdNS+NIR < PdNS, and PdNS+H₂O₂+NIR gave the highest inhibition rates (> 92.7%). Fifth, As determined by H&E staining of wound tissues on day 8 post-therapy (**Figure 6h** and **Figure S6h**, Supporting Information), PdNS+H₂O₂+NIR gave the best histopathologic outcome, i.e., abundant presence of fibroblasts (green arrow), newly-formed small blood vessels (red arrow), and regenerated hair follicles (black arrow), whereas there were still plenty of inflammatory cells (yellow arrow; such as neutrophils, lymphocytes, and macrophages) for all the other groups. Taken together, PdNS+H₂O₂+NIR gave the best *in vivo* antibacterial efficacy and wound healing outcome in a mouse model of acute wound infection.

2.6. Immunological and Transcriptomic Analysis of Host Response Posttherapy

To further dissect mechanisms of action of PdNS from the point of view of host response, inflammatory microenvironments at *S. aureus*-infected wound tissues on day 8 post different treatments were first assessed by immunohistochemical detection of the expression of pro-inflammatory cytokines IL-6 and TNF-α, which represented the 2 major positively correlated indicators of pro-inflammatory response at infected wounds.^[22,18] As presented in **Figure 7a–d**, the PdNS+H₂O₂+NIR gave the lowest expression of IL-6 and TNF-α indicating corresponding decrease in the level of inflammatory response, which is benefit from the lower bacterial load (**Figure 6g**). Second, immunofluorescent staining of *S. aureus*-infected wound tissues on day 8 post different treatments was conducted to measure the expression of 2 re-epithelialization factors EGF and KGF as the major contributors to stimulate epithelial cell proliferation (**Figure 7e–g**), 2

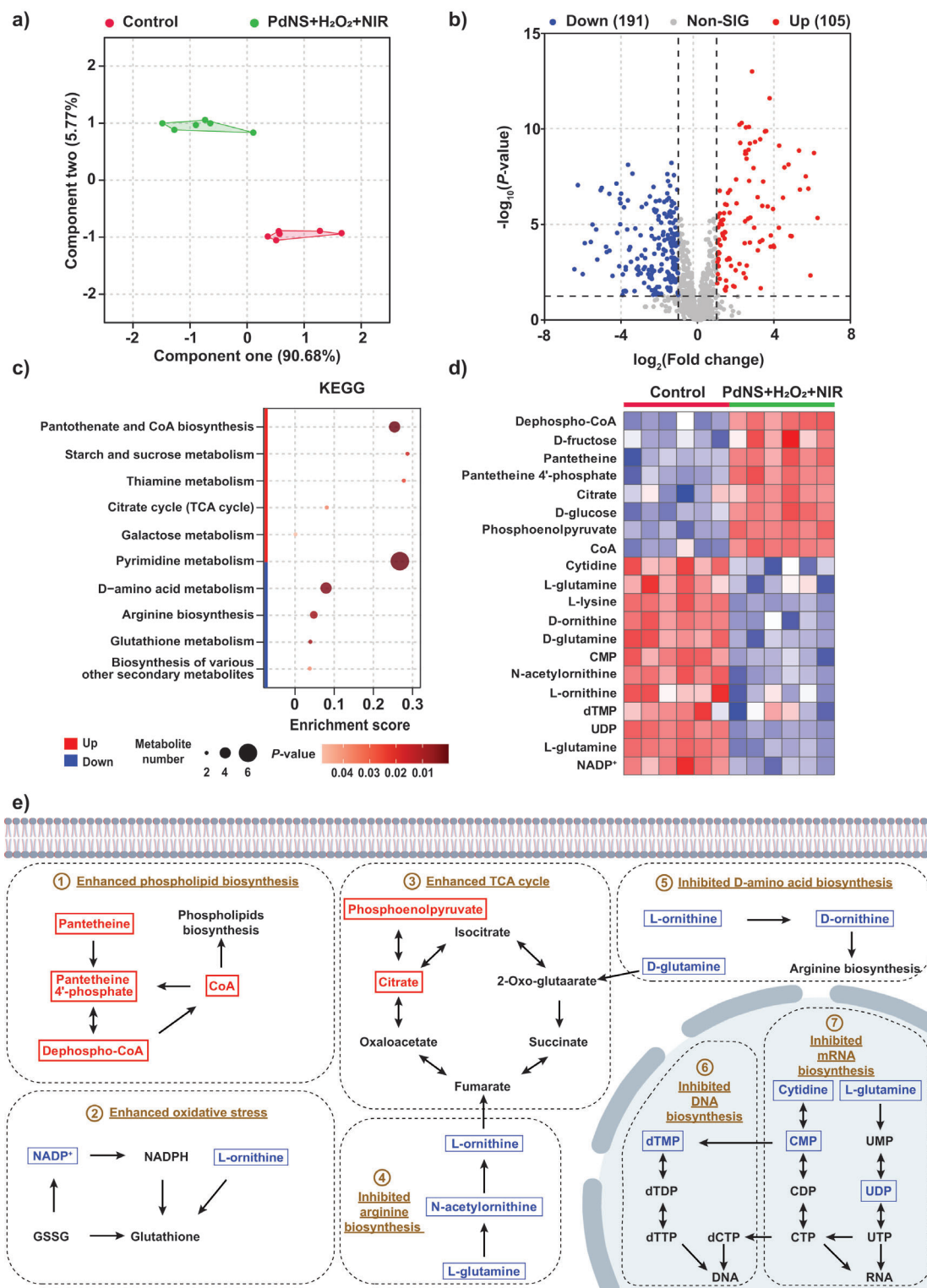


Figure 5. Metabolomics analysis of *S. aureus* after different treatments. a) PCA plot of clustered datasets between the two treatment groups PdNS+H₂O₂+NIR and Control. Control stands for PBS. PdNS corresponds to 50 μg mL⁻¹ PdNS. NIR represents 808 nm laser irradiation (1.5 W cm⁻², 3 min). H₂O₂ denotes the addition of 1 mM H₂O₂. b) Volcano plot of DRMs identified for PdNS+H₂O₂+NIR relative to Control. Up: Upregulated. Down: Downregulated. c) KEGG pathway enrichment analysis of DRMs. d) Heatmap of selected major DRMs and e) diagrams of corresponding biochemical processes. Red represents up-regulation and blue stands for downregulation. Experiments were performed with 6 independent biological replicates.

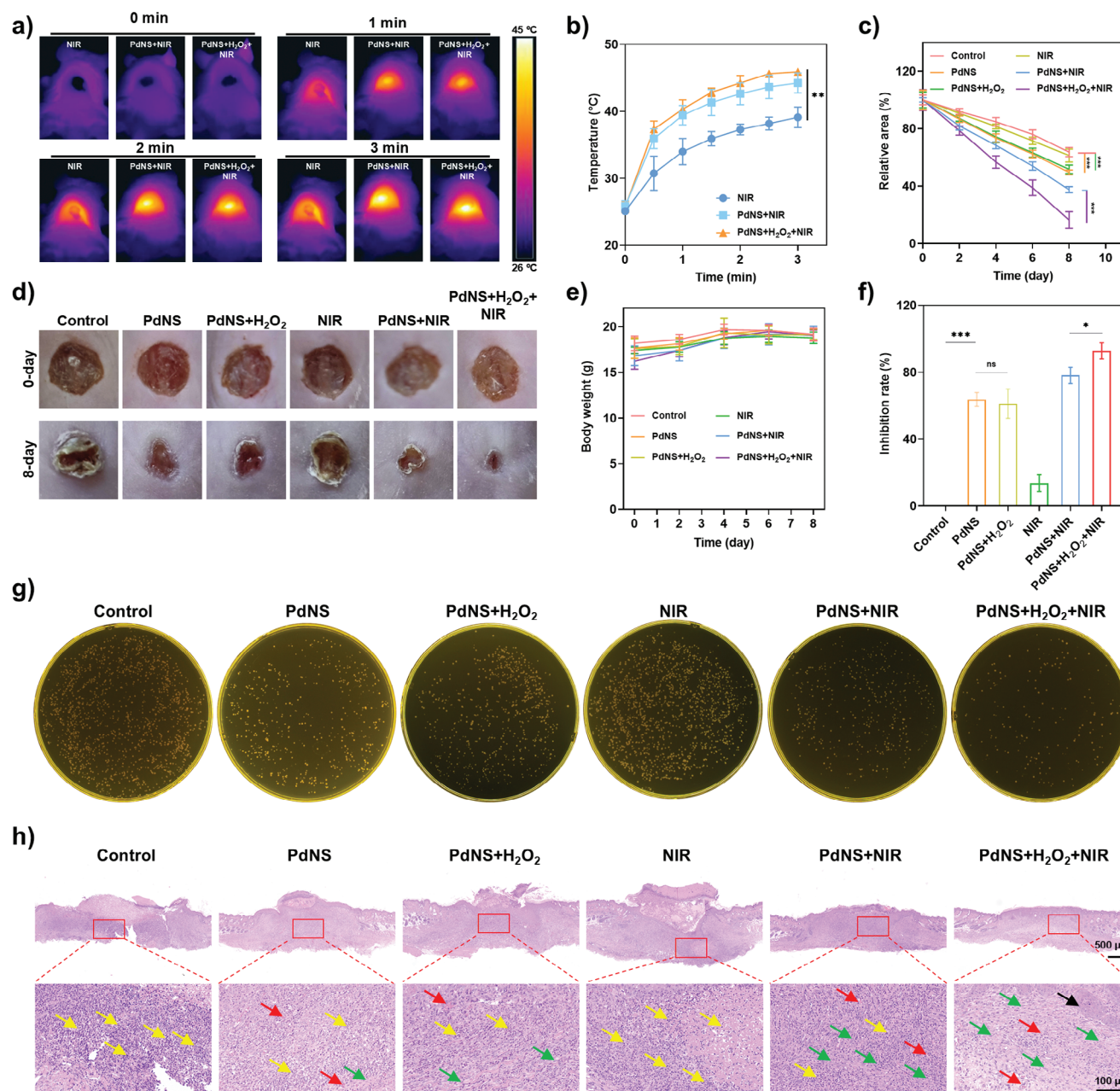


Figure 6. Therapeutic efficacy of PdNS against mice wounds infected by *S. aureus*. a) Infrared images at infected wounds post-therapy. b) Changes in local temperatures at infected wounds post-therapy. c) Statistical analysis of relative wound areas post-therapy. d) Representative photographs of infected wounds on day 0 and day 8 post-therapy. e) Body weights of mice post-therapy. f) Statistical analysis of bacterial load counts for infected wounds on day 8 post-therapy. g) Representative photographs of plate count agar for infected wounds on day 8 post-therapy. h) H&E staining of wound tissues on day 8 post-therapy. Green arrows: fibroblast cells. Red arrows: blood vessels. Black arrows: follicles. Yellow arrows: inflammatory cells. Control stands for PBS. PdNS corresponds to $50 \mu\text{g mL}^{-1}$ PdNS. NIR represents 808 nm laser irradiation (1.5 W cm^{-2} , 3 min). H_2O_2 denotes the addition of $1 \times 10^{-3} \text{ M H}_2\text{O}_2$. Data are presented as mean \pm SD ($n = 5$). ns: $P \geq 0.05$, *: $P < 0.05$, **: $P < 0.01$, ***: $P < 0.001$.

extracellular matrix (ECM) deposition factors collagen III (the main components of ECM) and α -SMA (the marker of myofibroblast cells as the major contributor to synthesize ECM) (Figure 7h–j), and 2 angiogenesis factors FGF-2 and VEGF-A (the major contributors to promote new blood vessel formation) (Figure 7k–m).^[26] As expected, the PdNS+ H_2O_2 +NIR gave the highest expression of each of these 6 proteins at wounds and

thus the maximum level of wound repair. The wound healing process can be divided into four major stages: I) Hemostasis; II) Inflammation; III) Proliferation; and IV. Maturation.^[26] As revealed by the above bacterial load counting, and histopathologic, immunohistochemical, and immunofluorescent staining results, PdNS+ H_2O_2 +NIR was at stage III characteristic of inhibited inflammatory response, and improved re-epithelialization, ECM

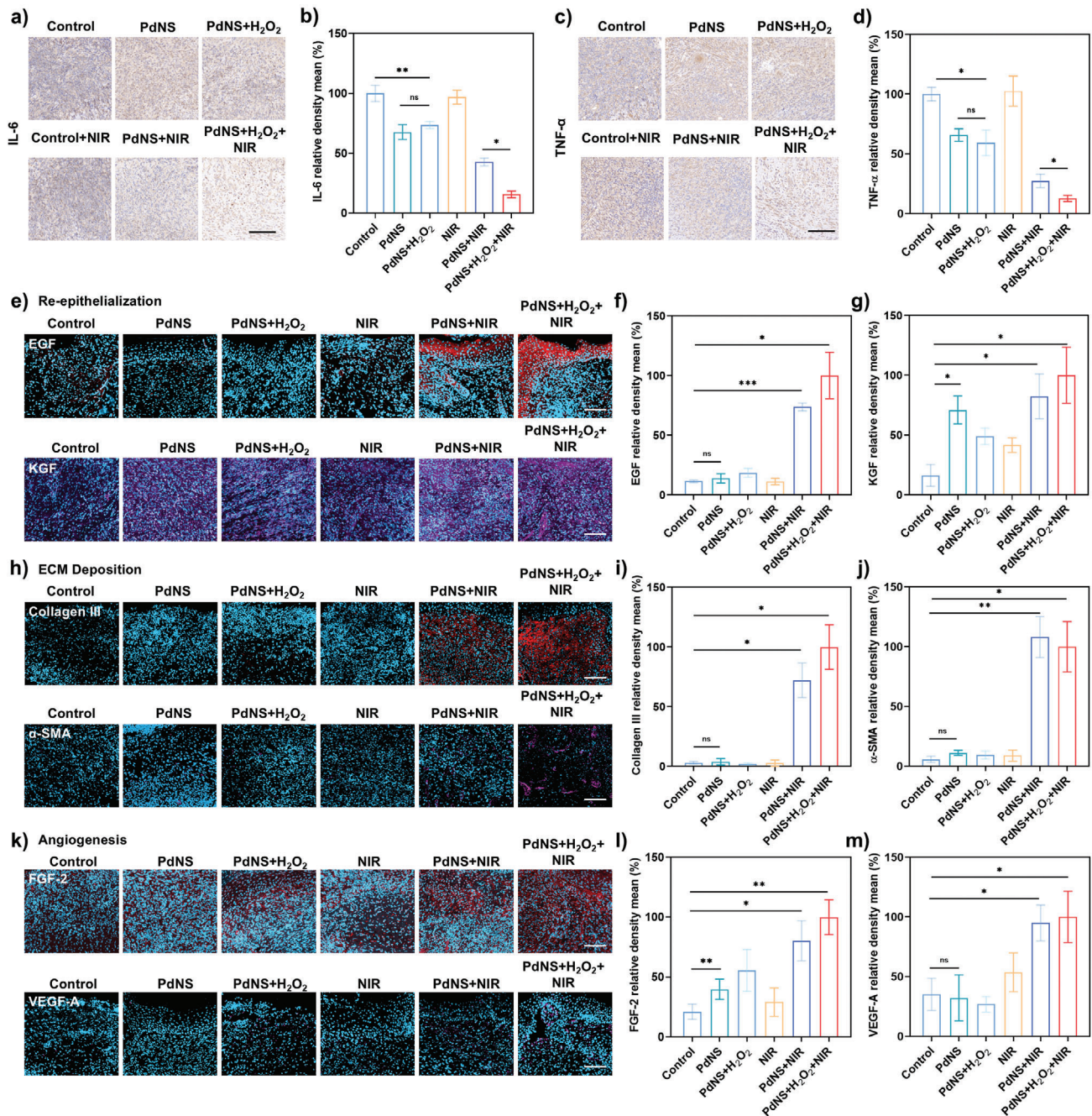


Figure 7. Immunohistochemical and immunofluorescent staining assays of infected wound tissues on day 8 post-therapy. a) Immunohistochemical staining of IL-6, and b) corresponding statistical analysis. c) Immunohistochemical staining of TNF- α , and d) corresponding statistical analysis. Immunofluorescent staining of e) EGF and KGF, and f,g) corresponding statistical analysis. Immunofluorescent staining of h) collagen III and α -SMA, and i,j) corresponding statistical analysis. Immunofluorescent staining of k) FGFR2 and VEGF-A, and l,m) corresponding statistical analysis. Scale bar is 100 μ m. Control stands for PBS. PdNS corresponds to 50 μ g mL⁻¹ PdNS. NIR represents 808 nm laser irradiation (1.5 W cm⁻², 3 min). H₂O₂ denotes the addition of 1×10^{-3} M H₂O₂. Data are presented as mean \pm SD ($n = 3$). ns: $P \geq 0.05$, *: $P < 0.05$, **: $P < 0.01$, ***: $P < 0.001$.

deposition, and angiogenesis; by contrast, all the other groups were at stage II, at which there was still abundant inflammation due to considerable bacterial loads.

To explore the global response of host gene transcription at *S. aureus*-infected wounds after phototherapy, the RNA-seq transcriptomes of infected wound tissues on 8 post-therapy were

compared between the PdNS+H₂O₂+NIR and Control groups (Figure 8). First, as shown in the PCA plot (Figure 8a), the clustered data sets of these 2 groups were far apart, and therefore there was a significant difference between these groups, and the data of 4 independent samples within each group were well repeated. Second, by analyzing the transcript levels of 14909

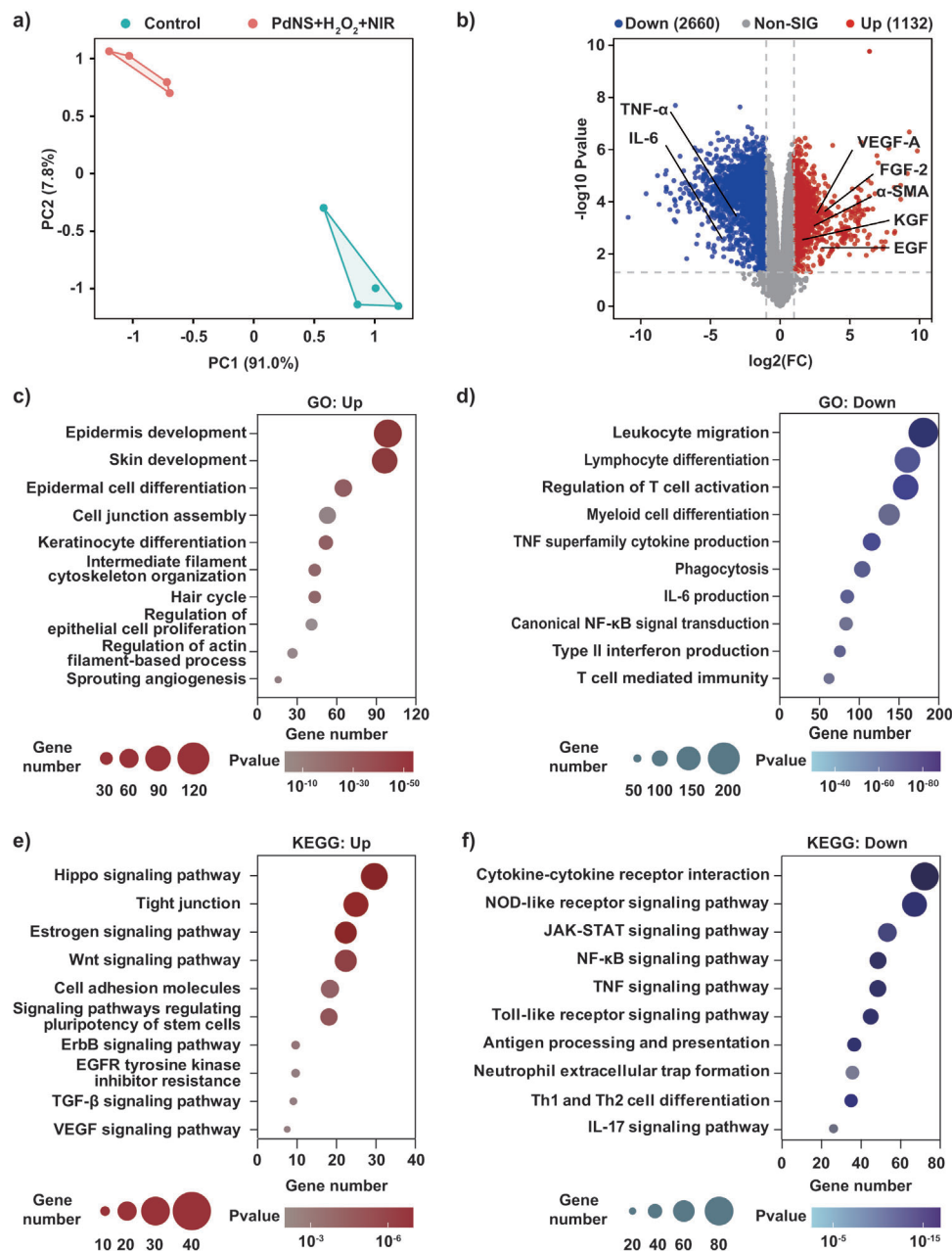


Figure 8. RNA-seq assay of *S. aureus*-infected wounds on day 8 post-therapy. a) PCA plot of clustered datasets between the PdNS+H₂O₂+NIR and Control groups. Control stands for PBS. PdNS corresponds to 50 μg mL⁻¹ PdNS. NIR represents 808 nm laser irradiation (1.5 W cm⁻², 3 min). H₂O₂ denotes the addition of 1 × 10⁻³ M H₂O₂. b) Volcano plot of differentially expressed genes for PdNS+H₂O₂+NIR compared to Control. Up: Upregulated genes. Down: Downregulated genes. GO pathway enrichment analysis was performed for c) downregulated and d) upregulated genes. Experiments are performed with 4 independent biological replicates.

genes at wound tissues, 3792 genes were identified to be differentially regulated in PdNS+H₂O₂+NIR compared to Control, of which 1132 were up-regulated and 2660 down-regulated (Figure 8b and Figure S11, Supporting Information). Notably, 5 (unexpectedly excluding collagen III) of the 6 wound-healing factors and both of the 2 pro-inflammatory cytokines, involved in the above immunological staining experiments, were included in these 1132 upregulated genes and 2660 downregulated genes, respectively. Third, as determined by Gene ontology (GO) path-

way enrichment analysis, the TOP 10 enriched up-regulated pathways were all related to epidermal regeneration and the dermal ECM deposition and angiogenesis (Figure 8c), while the TOP 10 enriched down-regulated pathways were all involved in the pro-inflammatory response (Figure 8d). KEGG pathway enrichment analysis gave similar results (Figure 8e,f). Fourth, a total of 23 up- or down-regulated genes from the above enriched pathways were illustrated by heatmap (Figure S11, Supporting Information), representing the major participants as viewed

from host gene expression response to accomplish the excellent therapeutic outcome of PdNS+H₂O₂+NIR. In conclusion, the PdNS+H₂O₂+NIR therapy could lead to the extensive down-regulation of pro-inflammatory pathways and the comprehensive up-regulation of wound healing pathways in mice, conferring the elevation of inflammation resolution and meanwhile the acceleration of wound repair.

3. Conclusion

This work developed a multi-functional single-component palladium nanosheet PdNS for photo-enhanced treatment of infected wounds caused by MDR bacteria. This single-component nanosheet structure shows the advantage of easy preparation, low cost, and high stability and controllability. PdNS exerted its endogenous nanoknife effect and peroxidase-like activity independent of light. This nanoknife effect would be attributed to not only the smaller particle size (about 48 nm) to facilitate the attachment of PdNS to the bacterial cell surface but also the extremely thin thickness (2–3 nm) to provide a prerequisite for the mechanical cutting into bacteria. Under NIR irradiation, PdNS exhibited the photothermal effect to produce local heat and meanwhile, the photodynamic effect to generate ¹O₂; in addition, PdNS showed extra photodynamic activity, which was inducible by its intrinsic catalase-like enzyme activity to generate O₂ upon H₂O₂ addition. By employing a collectively synergistic mechanism of nanoknife effect, peroxidase/catalase-like catalytic activity, photothermal effect, and photodynamic effect, PdNS+H₂O₂+NIR exhibited further >99.2% inhibition rates in vitro against MDR ESKAPE pathogens. The metabolomics analysis showed that PdNS+H₂O₂+NIR caused compensatory elevated phospholipid biosynthesis, disordered energy metabolism, increased cellular ROS levels and excessive oxidative stress, and inhibited nucleic acid synthesis in bacteria in vitro. In mice, PdNS+H₂O₂+NIR gave >92.7% bactericidal rates at infected wounds and almost the full recovery of infected wounds on day 8 post-therapy, and the immunological staining and transcriptomics assays showed that PdNS+H₂O₂+NIR lead to the extensive down-regulation of pro-inflammatory pathways and the comprehensive up-regulation of wound healing pathways, conferring elevated inflammation resolution and meanwhile accelerated wound repair. PdNS+H₂O₂+NIR represented a broad-spectrum and highly efficient nanoplatform for photo-enhanced treatment of superficial infections.

4. Experimental Section

Materials: Poly(vinylpyrrolidone) (PVP, MW = 30 000), Pd(acac)₂ (99%), and NaBr were purchased from Alfa Aesar. Ethanol and acetone were purchased from Sinopharm Chemical Reagent (China). N,N-dimethylformamide (DMF) was purchased from Aladdin, and 9,10-diphenylanthracene (DPA), methylene (MB), DMSO, and TEMP were purchased from Macklin. 3-(4,5-dimethylthiazol-2-yl)-2,5-diphenyltetrazolium bromide (MTT) Cell Proliferation Assay Kit and Hematoxylin and Eosin (H&E) Staining Kit were purchased from Beijing Solarbio (China). SYTO9/PI dye was purchased from Thermo Fisher (USA).

Preparation of PdNS: 300 mg of Pd(acac)₂, 960 mg of PVP, and 308 mg of NaBr were added to a stainless steel autoclave containing 15 mL of H₂O and 60 mL of DMF. The autoclave was purged with N₂ for 3 times.

The reactor was pressurized with CO to 0.5 MPa and heated at 90 °C for 3 h. After cooling to 0 °C in ice water, the obtained dark blue products were precipitated by acetone and separated by centrifugation. After being purified by a mixture containing ethanol and acetone, the obtained product was further dispersed in ethanol for 30 d, and PdNS was then obtained.

Statistical Analysis: All experiments were repeated at least 3 times and presented as mean ± SD. Asterisks indicate significant differences (ns: $P \geq 0.05$, *: $P < 0.05$, **: $P < 0.01$, ***: $P < 0.001$), analyzed by one-way ANOVA with Tukey post-hoc test.

Animal Ethical Clearance: All animal experiment protocols were reviewed and approved by the Institutional Animal Care and Use Committee of Beijing Institute of Microbiology and Epidemiology, Academy of Military Medical Sciences (Permit number: IACUC-DWZX-2022-026).

Supporting Information

Supporting Information is available from the Wiley Online Library or from the author.

Acknowledgements

S. L. and M. L. contributed equally to this work. This work was financially supported by the National Key Research and Development Program of China (Grant No. 2022YFC2603900); the Foundation of State Key Laboratory of Pathogen and Biosecurity of China (Grant No. SKLPBS2239); the National Natural Science Foundation of China (Nos. 22325801, U21A2085); Fundamental Research Funds for the Central Universities (No. QNTD2023-01, buctrc201915); the Postdoctoral Fellowship Program of CPSF under Grant Number GZB20240053.

Conflict of Interest

The authors declare no conflict of interest.

Data Availability Statement

The data that support the findings of this study are available from the corresponding author upon reasonable request.

Keywords

multidrug-resistant bacteria, nanosheets, photodynamic effect, photothermal effect, wound infection

Received: August 27, 2024
Revised: September 30, 2024
Published online:

- [1] J. M. A. Blair, M. A. Webber, A. J. Baylay, D. O. Ogbolu, L. J. V. Piddock, *Nat. Rev. Microbiol.* **2015**, *13*, 42.
- [2] a) D. M. P. De Oliveira, B. M. Forde, T. J. Kidd, P. N. A. Harris, M. A. Schembri, S. A. Beatson, D. L. Paterson, M. J. Walker, *Clin. Microbiol. Rev.* **2020**, *33*, e00181; b) G. Mancuso, A. Midiri, E. Gerace, C. Biondo, *Pathogens* **2021**, *10*, 1310.
- [3] M. Miethke, M. Pieroni, T. Weber, M. Brönstrup, P. Hammann, L. Halby, P. B. Arimondo, P. Glaser, B. Aigle, H. B. Bode, R. Moreira, Y. Li, A. Luzhetskyy, M. H. Medema, J.-L. Pernodet, M. Stadler, J. R. Tormo, O. Genilloud, A. W. Truman, K. J. Weissman, E. Takano, S. Sabatini, E. Stegmann, H. Brötz-Oesterhelt, W. Wohlleben, M. Seemann, M. Empting, A. K. H. Hirsch, B. Loretz, C.-M. Lehr, et al., *Nat. Rev. Chem.* **2021**, *5*, 726.

- [4] a) M. S. Mulani, E. E. Kamble, S. N. Kumkar, M. S. Tawre, K. R. Pardesi, *Front. Microbiol.* **2019**, *10*, 539; b) Y.-X. Ma, C.-Y. Wang, Y.-Y. Li, J. Li, Q.-Q. Wan, J.-H. Chen, F. R. Tay, L.-N. Niu, *Adv. Sci.* **2019**, *7*, 1901872.
- [5] S. Li, L. Shang, B. Xu, S. Wang, K. Gu, Q. Wu, Y. Sun, Q. Zhang, H. Yang, F. Zhang, L. Gu, T. Zhang, H. Liu, *Angew. Chem., Int. Ed.* **2019**, *58*, 12624.
- [6] a) A. K. Parameswaran, J. Azadmanjiri, N. Palaniyandy, B. Pal, S. Palaniswami, L. Dekanovsky, B. Wu, Z. Sofer, *Nano Energy* **2023**, *105*, 107994; b) A. Kumar, P. Choudhary, A. Kumar, P. H. C. Camargo, V. Krishnan, *Small* **2022**, *18*, e2101638.
- [7] Z. Li, B. Li, Q. Li, *Adv. Mater.* **2023**, *35*, 2211103.
- [8] J. M. V. Makabenta, A. Nabawy, C.-H. Li, S. Schmidt-Malan, R. Patel, V. M. Rotello, *Nat. Rev. Microbiol.* **2021**, *19*, 23.
- [9] P.-P. Li, H.-X. Wu, A. Dong, *Rare Met.* **2022**, *41*, 519.
- [10] C. Jia, F.-G. Wu, *BME Front.* **2023**, *4*, 0021.
- [11] L. Fan, A. Idris Muhammad, B. Bilyaminu Ismail, D. Liu, *Ultrason. Sonochem.* **2021**, *75*, 105591.
- [12] M. Awad, N. Thomas, T. J. Barnes, C. A. Prestidge, *J. Controlled Release* **2022**, *346*, 300.
- [13] H. Liu, F. Xing, Y. Zhou, P. Yu, J. Xu, R. Luo, Z. Xiang, P. M. Rommens, M. Liu, U. Ritz, *Mater. Des.* **2023**, *233*, 112231.
- [14] a) S. Wang, H. Zheng, L. Zhou, F. Cheng, Z. Liu, H. Zhang, L. Wang, Q. Zhang, *Nano Lett.* **2020**, *20*, 5149; b) J. Liu, R. S. Li, M. He, Z. Xu, L. Q. Xu, Y. Kang, P. Xue, *Biomaterials* **2021**, *277*, 121084; c) B. Jia, X. Du, W. Wang, Y. Qu, X. Liu, M. Zhao, W. Li, Y.-Q. Li, *Adv. Sci.* **2022**, *9*, e2105252.
- [15] S. Li, B. Xu, M. Lu, M. Sun, H. Yang, S. Liu, Z. Huang, H. Liu, *Adv. Mater.* **2022**, *34*, 2202609.
- [16] X. Liang, S. Qian, Z. Lou, R. Hu, Y. Hou, P. R. Chen, X. Fan, *Angew. Chem., Int. Ed.* **2023**, *62*, e202310920.
- [17] S. Wang, L. Shang, L. Li, Y. Yu, C. Chi, K. Wang, J. Zhang, R. Shi, H. Shen, G. I. N. Waterhouse, S. Liu, J. Tian, T. Zhang, H. Liu, *Adv. Mater.* **2016**, *28*, 8379.
- [18] X. Pan, N. Wu, S. Tian, J. Guo, C. Wang, Y. Sun, Z. Huang, F. Chen, Q. Wu, Y. Jing, Z. Yin, B. Zhao, X. Xiong, H. Liu, D. Zhou, *Adv. Funct. Mater.* **2022**, *32*, 2112145.
- [19] B. A. Diep, S. R. Gill, R. F. Chang, T. H. Phan, J. H. Chen, M. G. Davidson, F. Lin, J. Lin, H. A. Carleton, E. F. Mongodin, G. F. Sensabaugh, F. Perdreau-Remington, *Lancet* **2006**, *367*, 731.
- [20] C. M. Hudson, Z. W. Bent, R. J. Meagher, K. P. Williams, *PLoS One* **2014**, *9*, e99209.
- [21] H.-Y. Ou, S. N. Kuang, X. He, B. M. Molgora, P. J. Ewing, Z. Deng, M. Osby, W. Chen, H. H. Xu, *Sci. Rep.* **2015**, *5*, 8643.
- [22] M. Lu, S. Li, X. Xiong, Z. Huang, B. Xu, Y. Liu, Q. Wu, N. Wu, H. Liu, D. Zhou, *Adv. Funct. Mater.* **2022**, *32*, 2208061.
- [23] M. Hussein, E. K. Schneider-Futschik, O. K. A. Paulin, R. Allobawi, S. Crawford, Q. T. Zhou, A. Hanif, M. Baker, Y. Zhu, J. Li, T. Velkov, *ACS Infect. Dis.* **2020**, *6*, 1436.
- [24] P. J. Pomposiello, M. H. Bennik, B. Demple, *J. Bacteriol.* **2001**, *183*, 3890.
- [25] B. Peng, Y.-B. Su, H. Li, Y. Han, C. Guo, Y.-M. Tian, X.-X. Peng, *Cell Metab.* **2015**, *21*, 249.
- [26] a) H. N. Wilkinson, M. J. Hardman, *Open Biol.* **2020**, *10*, 200223; b) K. Raziyeve, Y. Kim, Z. Zharkinbekov, K. Kassymbek, S. Jimi, A. Saparov, *Biomolecules* **2021**, *11*, 700; c) G. C. Gurtner, S. Werner, Y. Barrandon, M. T. Longaker, *Nature* **2008**, *453*, 314.